We are IntechOpen,
the world's leading publisher of
Open Access books
Built by scientists, for scientists

4,800
Open access books available

122,000
International authors and editors

135M
Downloads

Our authors are among the

154
Countries delivered to

TOP 1%
most cited scientists

12.2%
Contributors from top 500 universities

CLARIVATE ANALYTICS
BOOK CITATION INDEX
INDEXED

WEB OF SCIENCE™

Selection of our books indexed in the Book Citation Index
in Web of Science™ Core Collection (BKCI)

Interested in publishing with us?
Contact book.department@intechopen.com

Numbers displayed above are based on latest data collected.
For more information visit www.intechopen.com

In-line Hard X-ray
Holography for Biomedical Imaging

Andrzej Krol

Department of Radiology, SUNY Upstate Medical University
Syracuse, NY
USA

1. Introduction

X-ray imaging for biomedical applications is based on detecting interactions of electromagnetic (EM) radiation with energy in the 15–200 keV range (corresponding to wavelength in the 0.8– 0.06 A range) with biological tissues. Such ultra short EM waves called x-rays can be generated through many different mechanisms (e.g. Bremsstrahlung in solid targets, characteristic x-ray emission, synchrotron radiation or in free-electron lasers) and may interact with biological objects being imaged via the coherent Rayleigh scattering, photoelectric absorption or Compton scattering. During x-ray imaging x-ray beam is directed on the object of interest and specially designed detectors detect the transmitted or scattered x-rays. Some x-ray detectors can count photons that interacted with the detector element while other simply record the average x-ray fluence over exposure time in a given detector element. Consequently, even though x-rays are EM radiation conventional detectors can only measure its amplitude but not phase. For biological tissues the complex refractive index is used to describe their interaction with x-rays. It is very close to unity and usually it is written as: $n = 1 – \delta – i\beta$, where the $\delta > 0$ (called the decrement of the real part of the refractive index) and $\beta > 0$ describe the phase and amplitude change of x-ray wave traversing tissue, respectively (Als-Nielsen & McMorrow, 2001; Lewis, 2004; Zhou & Brahme, 2008). In conventional x-ray imaging only information on attenuation (i.e. on the imaginary part β) is obtained. For water and soft tissue the ratio δ/β increases as a square of the x-ray energy up to $E\sim40$ keV and δ/β is in the 100–1200 range. The ratio δ/β is higher for lower effective Z compounds. Therefore, it is expected that effect of phase shift will be more pronounced in soft tissue imaging, as compared to bone. It follows that two x-ray waves traversing different biological tissues may exit the object with large phase difference even though the absorption they suffered was similar. Consequently, the ability to detect the x-ray phase shift during x-ray imaging could provide additional important information on the structure of the imaged object in addition to information on electron density that could be elucidated from conventional x-ray absorption imaging. The optimum energy for such phase-contrast imaging is higher than in absorption imaging possibly resulting in the radiation dose savings. We note that absorption–based x-ray imaging suffers from limited low-contrast resolution, i.e. the ability to differentiate two adjacent regions with similar electron density is rather poor. This can be remedied by use of imaging probes– contrast agents that provide higher or lower electron density around or in the structures of interest.

As an example, consider x-ray imaging of blood vessels (angiography). They cannot be detected while embedded in soft tissue by means of conventional absorption-based imaging unless iodinated contrast agent (e.g. Iohexol or Diatrizoate) is used. Typically only vessels with diameter larger than 200 μm could be detected. Unfortunately, use of contrast agents carries risk to some patients. Because x-ray phase shift is based on x-ray refraction rather than on absorption, blood vessels could be detected in phase-contrast imaging without any contrast agent or by using a new class of safer contrast agents. For example, Zhang et al. (2008) reported using in-line holography setup for imaging of blood vessels with 40 μm in diameter without any contrast agent and 30 μm vessels using physiological saline as contrast agent.

An important parameter that determines the character of phase contrast imaging is the Fresnel number $N_F=a^2/(\lambda z)$, where a is the size of the structure in the object being imaged, and z is the object-to-detector distance (Nugent et al., 2001). The far-field *(Frauenhofer region)*, intermediate-field Fresnel region and near-field Fresnel region can be defined as corresponding to $N_F\ll1$ $(z\gg a^2/\lambda)$, $N_F\approx1$ $(z\approx a^2/\lambda)$, and $N_F>1$ $(z<a^2/\lambda)$, respectively. The near-field region Fresnel region is especially important for biomedical imaging. In this regime the phase shift depends linearly on the object-to-detector distance and in most cases the phase variation can be expected to be continuous allowing to obtain unique solutions in well-defined domain and correctly-defined boundary conditions (Gureyev & Wilkins, 1998).

2. Common approaches to phase-contrast imaging

2.1 Triple crystal x-ray interferometry

This method relies on precisely aligned three lamellae (thin perfect Si crystals) cut from a single large Si monocrystal forming Bonse–Hart interferometer (Momose, 1995; Momose et al., 1996; Levis, 2004; Zhou & Brahme, 2008). The incoming x-ray beam is split by the first lamellae into two beams via Laue diffraction, the second lamellae diffracts the two beams onto the same spot on the third crystal where they interfere. The object of interest is placed in one of the beams (sampling beam) between the second and the third lamellae while the other beam is used as a reference and a phase shifter is inserted in it. The detector is placed in the optical path of the sampling beam emerging from the third lamellae. Because the phase shifter introduces known phase shift this device allows direct measurement of the phase map ($\cos\Phi(x,y)$) in the object. The spatial (lateral) coherence width and temporal coherence length that are necessary for this method are $\xi_s = \lambda (\Delta\alpha/\alpha)^{-1}$ and $\xi_t = \lambda (\Delta E/E)^{-1}$, respectively, where λ is the x-ray wavelength, $\Delta\alpha/\alpha$ is the device angular acceptance and $\Delta E/E$ is the x-ray energy bandpass of the device. For the Bonse–Hart interferometer the typical values are $\Delta\alpha/\alpha < 10^{-4}$ and $\Delta E/E< 10^{-4}$, therefore $\xi_s >10^{-6}$ m and $\xi_t >10^{-6}$ m resulting in coherence volume $V_c= \xi_s \times\xi_s \times\xi_t = 10^{-18}$ m^3. Such stringent coherence conditions can be only met by high brilliance x-ray source, e.g. synchrotron (Bilderback et al., 2005) or free-electron laser (Grubel et al., 2007) working in sufficiently short pulses, equipped with a crystal monochromator and by an interferometer made of a large single silicon crystal. The spatial resolution of a few micrometers was reported (Momose, 2002). The practical limitation for the wide spread of this technology is imposed by the need for a synchrotron or free-electron laser x-ray source, and rather small field-of-view (5×5 cm^2) created. This method is not suitable for imaging objects with very sharp interfaces (e.g. bone/soft tissue) because the resulting Fresnel fringes might become too narrow to be resolved by conventional detectors. However, this approach was successfully applied to 3D imaging of

small samples of soft tissues (e.g. rat brain, or excised breast tissue sample) resulting in 3D maps of the x-ray refractive index in the object reconstructed from multiple projections (Momose et al., 2003; Takeda et al., 2007).

2.2 Talbot interferometry

Talbot interferometry (Yokozeki & Suzuki, 1971; Lohmann & Silva, 1971) is based on the Talbot effect (Weitkamp et al., 2005; Momose et al., 2006). The imaging system consists of a phase grating G1 and an analyzer absorption grating G2 very close to the detector. If an x-ray source with low spatial coherence is used, an additional source grating G0 is inserted between the x-ray source and the object located in front of G1 (Weitkamp et al., 2006; Pfeiffer et al. 2006). If the distance between G1 and G2 is equal to the Talbot distance, the phase grating creates periodic fringe (moiré) pattern on G2 via Talbot effect. The period of G2 needs to match the period of the moiré pattern. For weakly absorbing objects the recorded image is directly related to gradient of phase, $d\Phi(x,y)/dx$, where x and y are perpendicular to the x-ray propagation vector and x is in the transverse direction perpendicular to gratings' slits. The phase shift in the object can be estimated by integration along the x-axis. Better approach is to translate G1 or G2 in the x direction and to obtain at least four images. In such way one can obtain information on the absorption component and on the phase-shift component of the image. For Talbot interferometry the required spatial coherence is $\xi_s = \lambda l/w \sim 10^{-8}$, where l is the G0–G1 distance and w is the source size. Because $\Delta E/E < 10^{-1}$, therefore temporal coherence is $\xi_t > 10^{-9}$, thus offering most relax coherence conditions ($V_c = 10^{-25}$ m^3) among all phase contrast imaging methods. The spatial resolution is defined by the source size and magnification via $\sim wd/l$, where d is the G1–G2 distance. The advantage of this method is that it could be used with conventional medical x-ray tubes and conventional large field-of-view x-ray detectors. The disadvantage is the limited grating size (presently not exceeding 10 cm×10 cm) thus resulting in the limited field-of-view, limited angular acceptance that may extend the required imaging time while working with the cone-beam source (such as x-ray tube). Presence of three gratings inserted between the x-ray source and the detector may result in dose increase to the patient (Olivo & Speller, 2007).

2.3 X-ray diffraction-enhanced imaging and multi-image radiography technique

X-ray diffraction-enhanced imaging (DEI) system consists of a crystal monochromator and a silicon single crystal analyzer. The analyzer is aligned with the monochromator in such a way that the x-rays with angular incidence within the rocking curve width relative to the Bragg angle of analyzer are accepted. The object is inserted between the monochromator and the analyser crystal. If the rocking angle is set at the half of the maximum reflectivity (larger or smaller than the Bragg angle) than the images recorded by the detector will contain information about gradient of phase shift $d\Phi(x,y)/dx$ and also about absorption of the object. If the rocking angle is set to be equal to the Bragg angle only information about absorption of the object will be provided (Chapman et al., 1997). By obtaining multiple images at low and high angles about the Bragg angle one can retrieve information on the imaginary part and on the gradient of the real part of the x-ray refracting index of the object. Because in this imaging setup under some conditions one can also obtain images due to ultra-small-angle scattering, therefore this method was expanded to multi-image radiography (MIR) technique (Wernick et al., 2003; Rigon et al., 2007). MIR requires acquisition of multiple images at different angular settings and appropriate reconstruction

methods. The estimated coherence volume for DEI is about 10^{-18} m³, therefore this method can be only implemented with very high brilliance x-ray source such as synchrotron or free-electron laser x-rays source. The reported spatial resolution was in the range of a few micrometers (Nesterets et al., 2004). Another limitation of this method stems from the fact that the x-ray beam emerging from the analyzer is vary narrow (typically no more than 1 mm height) with its width not exceeding 10 cm. Therefore only relatively small objects can be imaged via sample scan. Such approach might result in motion artifacts and is technically challenging.

2.4 In-line hard x-ray holography

The in-line holography also called propagation-based imaging does not require any diffracting crystals or gratings. It is the simplest approach to phase contrast imaging. It was first investigated by Snigirev et al. (1995), and Wilkins et al. (1996). This method requires sufficiently small x-ray source to fulfil the condition for spatial coherence $\xi_s > 10^{-6}$ m. However, a broad x-ray spectrum $\Delta E/E < 10^{-1}$ is adequate leading to relaxed condition for temporal coherence $\xi_t > 10^{-9}$ m (Wilkins et al., 1996). The geometry used is shown in Fig. 1.
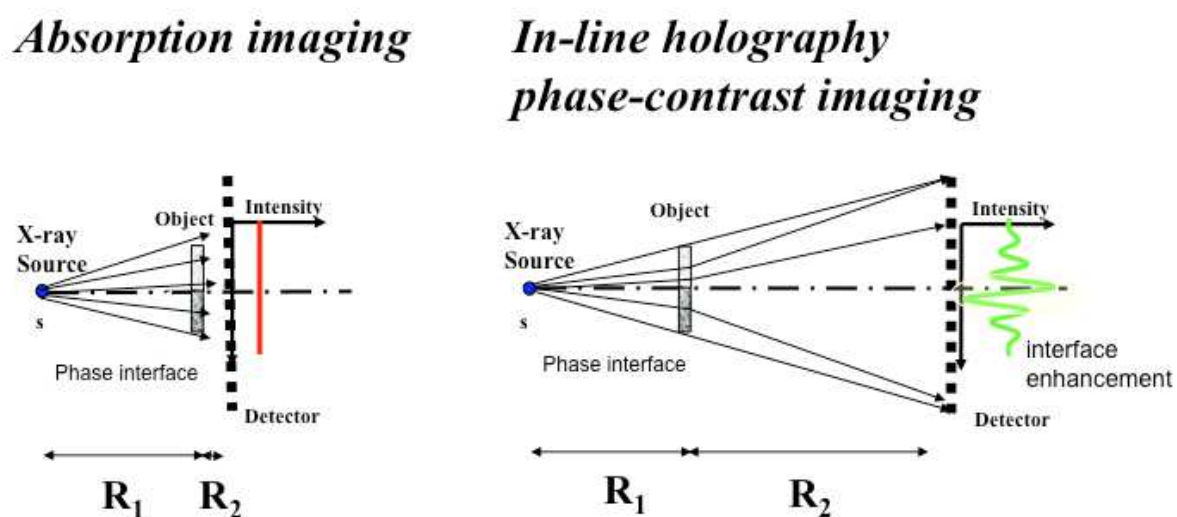

Fig. 1. Left panel: imaging geometry for absorption imaging. Right panel: imaging geometry for in-line holography setup. Absorption imaging setup does not allow detecting a phase interface in the object. In-line holography setup under some conditions might allow detection of a phase interface in the object.

The R_1 and R_2 denote the source-to-object and the object-to-detector distance, respectively. For the in-line holography the spatial coherence width condition can be expressed as

$$\xi_s = \lambda \,(\Delta\alpha/\alpha)^{-1} = \lambda(s/R_1)^{-1} = \lambda(R_1/s), \tag{1}$$

where s is the x-ray effective source size. Wu and Liu (2007) proposed a measure for estimation of the degree of coherence required to create detectable phase-contrast. Based on Wigner distribution function they introduced concept of the shearing length $L_{shear} = \lambda R_2 |u|/M$, where u is the spatial frequency of the object. They pointed out that the ratio

$$L_{shear}/ \xi_s = R_2 |u| /MR_1 = (M-1)s|u|/M \qquad (2)$$

is a better measure of coherence of the x-ray wavefield within the shearing length for a given spatial frequency u. For $L_{shear}/ \xi_s << 1$, the wavefield is highly coherent over the shearing length. It follows, that the shortest spatial wavelength (λ_o) of the object component that could be imaged via phase contrast is defined by

$$\lambda_o >> s(M-1)/M = s'/M, \qquad (3)$$

where s' is the size of projected source on the detector plane (geometrical unsharpness of the system). If $L_{shear}/ \xi_s \geq 1$ or $\lambda_o \leq s'/M$ than phase contrast cannot be detected. It is interesting that the above conditions do not depend on x-ray energy.

Wilikins et al. (1996) and Pogany et al. (1997) showed that for in-line holography of weakly absorbing objects in the near-field Fresnel region the observed image contrast is proportional to the Laplacian of the phase-shift ($d^2\Phi(x,y,z)/dxdy$) thus it is proportional to the Laplacian of projected electron density in the object. Consequently, only large variations in projected electron density i.e. large phase gradients ("sharp" interfaces) will significantly contribute to phase-shift-related image contrast. It this case the phase contrast is practically independent of energy.

3. Figure-of-merit for in-line holography phase-contrast imaging with cone-beam x-ray source

For laboratory-based applications of in-line holography only compact size x-ray sources need to be considered. They include microfocal x-ray tube and ultrafast-laser based plasma x-ray source (Kieffer et al., 2002). Such sources work in cone-beam geometry (Fig. 1). Hereafter, we will discuss optimization of geometrical parameters of such systems.

In order to optimize image quality in phase-contrast imaging we need to maximize the signal-to-noise ratio (SNR_A) for a given feature (A) in the object at a fixed absorbed dose (Krol et al., 2007). We introduce the following figure–of–merit that has to be maximized:

$$FOM_A = SNR_A |_{Dose=const} \qquad (4)$$

One can define the image signal (S_A) as an absolute difference between the measured x-ray intensities in the image plane with and without the feature of interest, integrated over a selected region (A) in the image plane.

$$S_A = \int_A dxdy \, | \int_0^\infty dv \Big[F_{obj}(x,y;v) - F_{bg}(x,y;v) \Big] \eta(v)| \qquad (5)$$

where A is the region in the image plane for which the signal is measured, F_{obj} and F_{bg} are the x-ray fluences (photons per unit area) per unit bandwidth in the image plane with and without the feature of interest, respectively, (x,y) are the Cartesian coordinates in the image plane, v is the x-ray frequency ($v=c/\lambda$), where c is the speed of light and λ is the x-ray wavelength) and $\eta(v)$ is the quantum efficiency of the detector. We can rewrite (5) in a form

$$S_A = \iint_A dxdy \, | I_{obj}(x,y) - I_{bg}(x,y)| \qquad (6)$$

where $I_{\mathrm{obj}}(x,y) = \int_0^\infty d\nu F_{\mathrm{obj}}(x,y;\nu)\eta$ is the time-integrated intensity of the image and

$I_{\mathrm{bg}}(x,y) = \int_0^\infty d\nu F_{\mathrm{bg}}(x,y;\nu)\eta(\nu)$ is the background intensity. They are defined as detector

counts per unit area. Therefore, it is a dimensionless quantity.

Because x-ray generation follows Poisson statistics, the noise can be expressed as

$$N_A = T_A^{1/2} \tag{7}$$

where $T_A = \int\limits_A dxdy\left[I_{obj}(x,y) + I_{bg}(x,y) \right]$ is the total number of detector counts acquired in

region A.

Consequently, the recorded signal-to-noise ratio is

$$SNR_A \equiv \frac{S_A}{N_A} = \frac{S_A}{T_A^{1/2}} \tag{8}$$

The region A over which the signal is measured is defined differently for the phase-shift-than for the absorption-related contrast. In the case of signal due to absorption, S_A^a, the natural choice of the region A is the whole image of the feature, $A=\Omega$, while in the case of the near-field Fresnel region in-line phase-contrast signal, S_A^φ, the natural choice is a strip Γ around the image of the boundary of the feature A with its width proportional to the width of the first Fresnel fringe (Fig. 2). For this reason, we modify definition of the SNR_A to make it suitable to describe in-line phase-contrast imaging:

$$SNR_A = \sqrt{\left(\frac{S_\Gamma^\phi}{N_\Gamma} \right)^2 + \left(\frac{S_\Omega^a}{N_\Omega} \right)^2} \tag{9}$$

Our goal is to maximize the SNR_A for a given feature A in the object at a fixed absorbed radiation dose. The absorbed dose is uniquely determined by the object radiological properties and the spectral distribution of the incident x-ray beam. Therefore, the incident fluence $F_{\mathrm{in}}(x',y';\nu) \equiv F_{\mathrm{in}}(\nu)$ is uniquely fixed by the dose. For a given x-ray spectrum we can only vary geometrical parameters of the imaging setup for the purpose of SNR maximization. In order to keep the incident fluence constant when the source-to-object distance R_1 is varied, the exposure time or the x-ray source intensity needs to be varied appropriately. Under assumption that in the vicinity of the feature of interest the incident x-ray fluence $F_{\mathrm{in}}(x',y';\nu)$ and the projected x-ray absorption coefficient in the object $E_{\mathrm{obj}}(x',y';\nu)$ are slowly varying as functions of transverse coordinates (x',y'). and the x-ray frequency ν, and at a fixed incident fluence, the signal and noise corresponding to x-ray absorption will be practically independent of imaging geometry as the decrease in photon fluence in the image plane as a function of the object-to-detector distance R_2 will be compensated by the corresponding change in system magnification resulting in increase of the projected feature area. Consequently, only SNR_A^φ i.e. SNR_A corresponding to the phase –shift contribution to image contrast needs to be maximized,

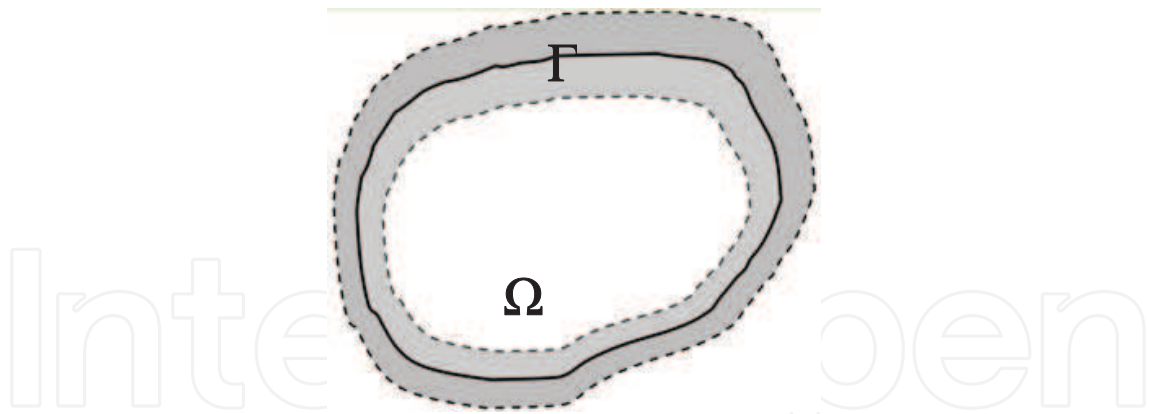$$SNR_A^\varphi = \frac{S_\Gamma^\phi}{N_\Gamma}, \tag{10}$$

Fig. 2. Schematic depiction of the feature of interest A: Ω is the region inside the solid line (image of the feature of interest); Γ is the region between the dashed and solid lines (a strip around the boundary of the feature of interest).

We will examine $SNR_A{}^{\varphi}$ characteristics as a function of geometrical parameters of the imaging setup and we will show that it exhibits more complex behavior, as compared to the absorption $SNR_A{}^a$. Following the assumption that the incident fluence and the object absorption properties are slowly varying in the vicinity of the feature of interest, one can also assume that the background intensity is also as slowly varying function of transverse coordinates in the vicinity of the image of the feature. Therefore, $I_{bg}(x,y) \equiv I_{bg}$ and $\iint_{\Gamma} dxdy I_{bg}(x,y) = |\Gamma| I_{bg}$, where $|\Gamma|$ is the area of the Fresnel fringe strip Γ. Because the phase shift does not change the integrated intensity of the image, one can make use of the approximation $\iint_{\Gamma} dxdy I_{obj}(x,y) \cong |\Gamma| I_{bg}$. We recall that the background intensity I_{bg} decreases as the inverse of the square of magnification, $I_{bg} \sim M^{-2} I_{in}$, while the intensity incident on the object (I_{in}) is fixed by the dose. Substituting these expressions into (4), we obtain an expression for the Figure of Merit (FOM) that has to be maximized:

$$FOM = \frac{S_{\Gamma}^{\varphi} M}{\sqrt{|\Gamma| I_{in}}} = \gamma\, S_{\Gamma}^{\varphi}\, |\Gamma|^{-1/2}\, M \,, \tag{11}$$

where $\gamma \sim I_{in}^{-1/2}$ is a constant that depends on the object and the x-ray spectrum (because for different incident x-ray spectra the same dose may correspond to different incident intensities), but not on the geometric characteristics of the imaging setup. For the in-line holography imaging system

$$\Gamma \cong 2M\sigma_M , \text{ and } \sigma_M^2 \equiv \sigma_{obj}^2 + \sigma_{sys}^2(M) = \sigma_{obj}^2 + (M-1)^2 M^{-2} \sigma_{src}^2 + M^{-2} \sigma_{det}^2 , \tag{12}$$

where σ_{obj} describes the "unsharpness" of the object boundary, σ_{src} and σ_{det} are the standard deviations of the source intensity distribution and the detector point-spread-function (PSF), respectively, and M is the geometric magnification. Because the strip Γ is defined by the first Fresnel fringes at both sides of the boundary, its area is

$$|\Gamma| \cong 4M^2 \sigma_M L = 4M^2 L \left[\sigma_{obj}^2 + \sigma_{sys}^2(M) = \sigma_{obj}^2 + (M-1)^2 M^{-2} \sigma_{src}^2 + M^{-2} \sigma_{det}^2 \right], \tag{13}$$

where L is the length of the boundary of the feature of interest. Let us introduce the incident intensity-independent average phase-shift image contrast $\overline{C}_\Gamma^\varphi$ over Γ

$$\overline{C}_\Gamma^\varphi \equiv S_\Gamma^\varphi / T_\Gamma, \tag{14}$$

where $T_\Gamma \equiv T_{A=\Gamma}$ is the total number of detector counts in the strip Γ.

By substituting (13) and (14) into (11) one obtains:

$$FOM = \gamma' \, \sigma_M^{-1/2} \, S_\Gamma^\varphi = \gamma'' \, \sigma_M^{1/2} \, \overline{C}_\Gamma^\varphi, \tag{15}$$

where $\gamma' \sim (LI_{in})^{-1/2}$ is a constant that depends on the object feature and the x-ray spectrum, but not on the geometric parameters of the imaging system, and $\gamma'' \equiv \gamma' T_\Gamma \sim (LI_{in})^{1/2}$ is another constant. Equation (8) allows practical optimization of geometrical parameters for the in-line holography with cone-beam x-ray source.

A universal analytical expression for the phase-contrast signal, S_Γ^φ and for the phase-shift contrast $\overline{C}_\Gamma^\varphi$, is difficult to derive because it depends on a number of factors including the shape and sharpness of the boundary of Ω. In general, these two parameters depend on of geometric parameters of the imaging setup.

Hereafter, we will optimize the FOM defined by (11) for some simple objects.

4. Examples of applications

4.1 In-line holography imaging of nylon fibers: system geometry optimization

An example of optimization of in-line holography setup for specific application – nylon fibers imaging – can be found in Krol et al., (2007). An image of Nylon fibers (10–330 µm diameter) obtained with ultrafast laser operating at 100 Hz, 28 fs and 40 mJ perpulse and x-ray focal spot size 10 µm (Advanced Laser Light Source [ALLS] Laboratory, Institut National de la Recherché Scientifique, University of Quebec, Canada), with Mo targets and Be filter are shown in Fig. 3 Projection images of nylon fibers of 10–330 µm diameter were obtained in in-line holography setup using an ultrafast laser-based x-ray source. [Krol et. al, 2007]
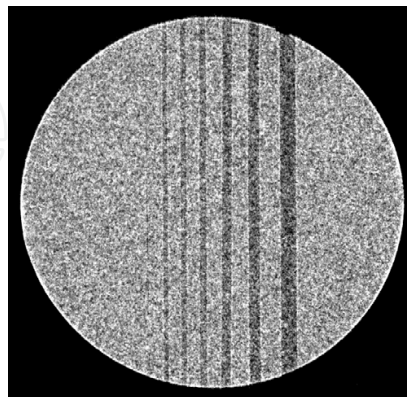

Fig. 3. Normalized image of nylon fiber phantom acquired at ALLS laboratory (INRS) with 100 Hz ultrafast laser-based x-ray source with Mo target and Be filter. Source-to-object distance, R_1 = 40.7 cm; source-to-detector distance R_2 = 48.9 cm; magnification M = 2.201. A cooled CCD camera (24 µm pitch) was used with a Gd_2OS_2 screen coupled via 1:1 optical taper.

Comparison of experimental line profiles through images of Nylon fibers shown in Fig. 3 with simulations are shown in Fig. 4 (Nesterets et al., 2005). We observe satisfactory agreement between experiment and theory. It should be stressed that no curve fitting was performed, nor was any "fudge factor" used. These results confirmed applicability of the theoretical model for Nylon fibers in-line holography phase-contrast imaging simulations.
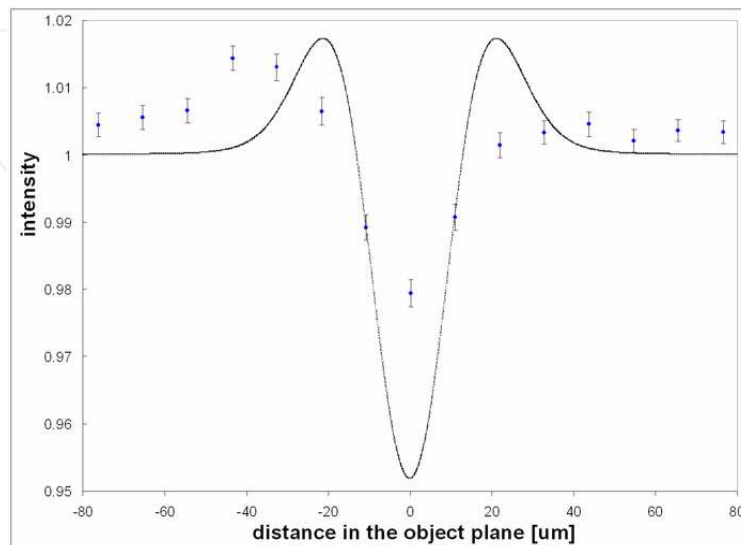
(a)
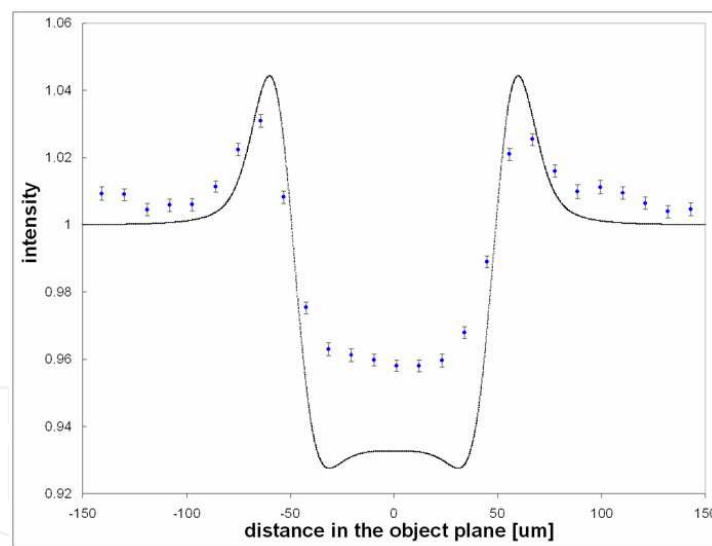
(b)

Fig. 4. Comparison of experimental line profiles through the images of Nylon fibers obtained with 100 Hz ultrafast laser at 50% power level, at ALLS-INRS lab. The solid lines represent the theoretical calculations. The discrete data points are taken from experiments using a CCD detector (24 μm pitch) with Gd_2OS_2 screen. (a) Nylon fiber with 20 μm diameter, Mo target, Be filter, R_1 = 40.7 cm, R_2 = 48.9 cm. (b) Nylon fiber with 100 μm diameter, Mo target, Be filter, R_1 = 40.7 cm, R_2 = 48.9 cm.

The rigorous wave-optical formalism was used to estimate S_Γ^φ and $\overline{C}_\Gamma^\varphi$ in (8). The following four parameters were estimated:

Contrast:

$$Contrast = \frac{I_{\max} - I_{\min}}{I_{\max} + I_{\min}} \tag{16}$$

where I_{max} and I_{min} are the adjacent minimum and maximum of the intensity due to phase shift in the first Fresnel fringe image of the object.

Signal-to-noise ratio:

$$SNR = \frac{\int\limits_{\Omega} |I_{obj} - I_{bg}| dS}{\left(\int\limits_{\Omega} [I_{obj} + I_{bg}] dS \right)^{1/2}} \tag{17}$$

where the region Ω in the image is chosen such that it contains 90% of the total signal $\int\limits_{\Omega} |I_{obj} - I_{bg}| dS$ and I_{obj} and I_{bg} are fluencies trough the object and the background at the image plane, respectively.

Resolution is defined as the distance between the adjacent minimum and maximum of the intensity in the image of the object due to phase shift in the first Fresnel fringe and divided by the magnification *M*.

Sampling is defined as the distance (d_F, in pixels of the detector) between the adjacent minimum and maximum of the intensity due to phase shift in the first Fresnel fringe image of the object.

We have investigated the influence of the geometrical parameters of the imaging setup on the characteristics of the phase-contrast images of Nylon fibers (Krol et al., 2007). We assumed Gaussian spatial intensity distribution of the source with FWHM$_S$ = 5 µm and Gaussian resolution function of the detector with FWHM$_D$ = 50 µm. We calculated dependences of the *Contrast*, *SNR*, *Resolution* and *Sampling* on the magnification *M* assuming the total source-to-detector distance to be fixed at *R* = 2 m (Figs. 5 and 6).
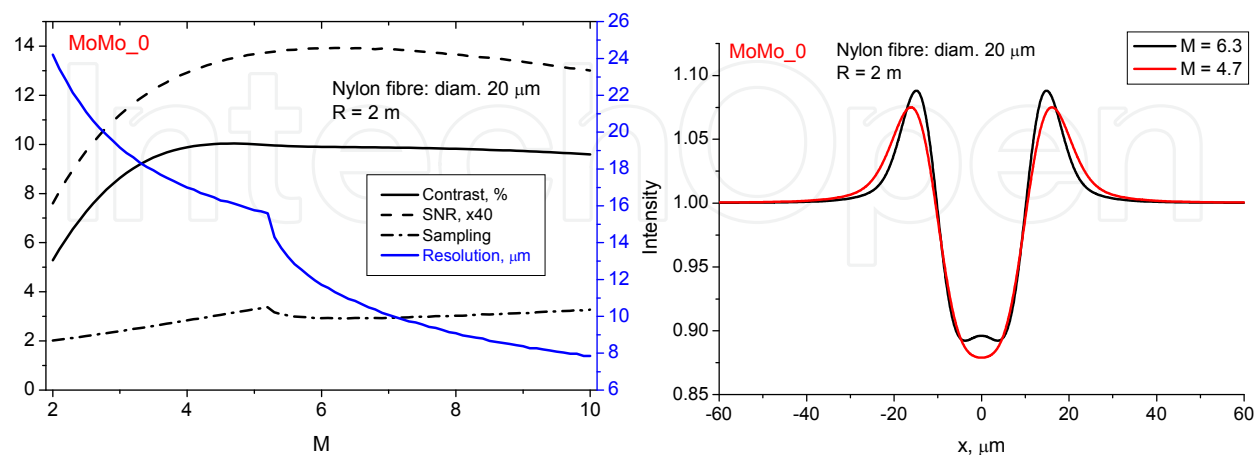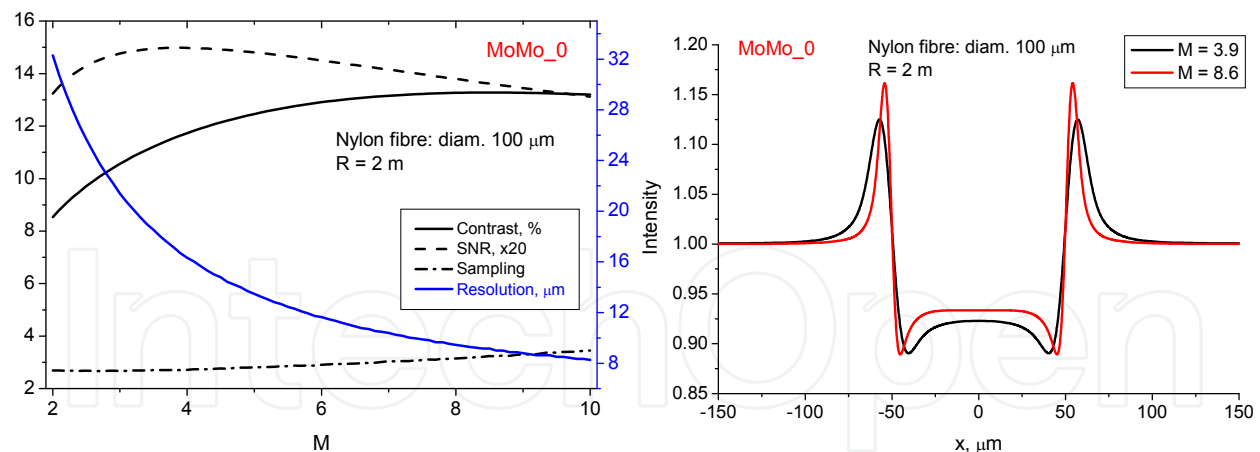

Fig. 5. Left panel: Calculated dependences of the Contrast, SNR, Resolution and Sampling on the magnification *M* at the total source-to-detector distance fixed at R = 2 m. Right panel: Calculated line profiles at magnification M=6.3 and M=4.7. ULX spectrum is obtained with Mo target and Be filter only.

Fig. 6. Left panel: Calculated dependences of the Contrast, SNR, Resolution and Sampling on the magnification M at the total source-to-detector distance fixed at $R = 2$ m. Right panel: Calculated line profiles at magnification M=3.9 and M=8.6. Ultrafast laser-based x-ray source spectrum is obtained with Mo target and Be filter.

Analysis of Figs. 5 and 6 indicates that contrast and SNR vs. magnification exhibit broad maxima and that variation of M_C with fiber diameter is relatively small (7.7 – 8.6 for 10 –100 μm fiber diameter, respectively) while M_{SNR} changes significantly (7.7 – 3.9 for 10 –100 μm fiber diameter, respectively). The maximum contrast is almost independent of the fiber diameter (10.7% –13.2% for the 10 – 100 μm fiber diameter, respectively), while the maximum of SNR rapidly increases with increase of the fiber diameter (0.2461 –0.7492 for the 10 – 100 μm fiber diameter, respectively).

Let $R_1 = R/M$ be the source-to-object distance with R_1 and R_2 variable and $R=R_1+R_2=const$. We wish to optimize FOM defined in (4), In order to keep the dose constant when R_1 is varied, the exposure time or the x-ray source intensity has to be varied accordingly.

We conclude that:

i. The optimum magnification (which maximizes the *FOM*) is almost independent of the total source-to-detector distance, *R*, and depends only on the properties of the imaged object, the source size and the detector resolution.

ii. The corresponding maximum values of the contrast and *SNR* are almost linear with respect to *R*

iii. The optimum magnification decreases with fiber diameter;

iv. The minimum fiber diameter defines the minimum source-to-object distance R_1, if *R* is fixed and the object is moved.

These conclusions allow us to propose the following strategy for choosing the optimum geometry for phase-contrast imaging: First, for a given object feature type one should calculate the optimum magnification M^{opt} that maximizes the FOM. Second, assuming that *R* is fixed, calculate the optimum source-to-object distance as $R_1^{opt} = R/M^{opt}$.

Similar calculations were performed for in-line holography system with fixed R_1 and variable R_2 $(R=R_1+R_2)$, where *R* is the total source-to-detector distance. The results show that M_C is almost independent of the *R* while M_{SNR} rapidly increases with *R*. Both parameters strongly depend on the radius of a fiber. For fixed R_1 and R_2 they increase with the fiber diameter.

Investigation of the influence of x-ray spectrum mean energy on *SNR* and contrast indicate that these two parameters decrease with increasing mean x-ray energy.

4.2 Soft tissue small avascular tumor imaging with x-ray phase-contrast micro-CT in-line holography setup

In-line holography phase-contrast imaging might allow detection and quantification of soft tissue tumors that cannot be imaged using conventional absorption radiography. We analyzed feasibility of small soft tissue avascular tumor in mouse model imaging with x-ray phase-contrast using in-line holography setup and compared its performance with absorption-based imaging (Nesterets et al., 2008). We simulated imaging of a small spheroidal avascular invading tumor in mouse model in an early stage of development, i.e. not containing a necrotic core (Jiang et al., 2005, Stein et al., 2007) with quiescent cell core (smaller than 250 µm) and a range of distributions of the proliferating cell density forming the outer shell.
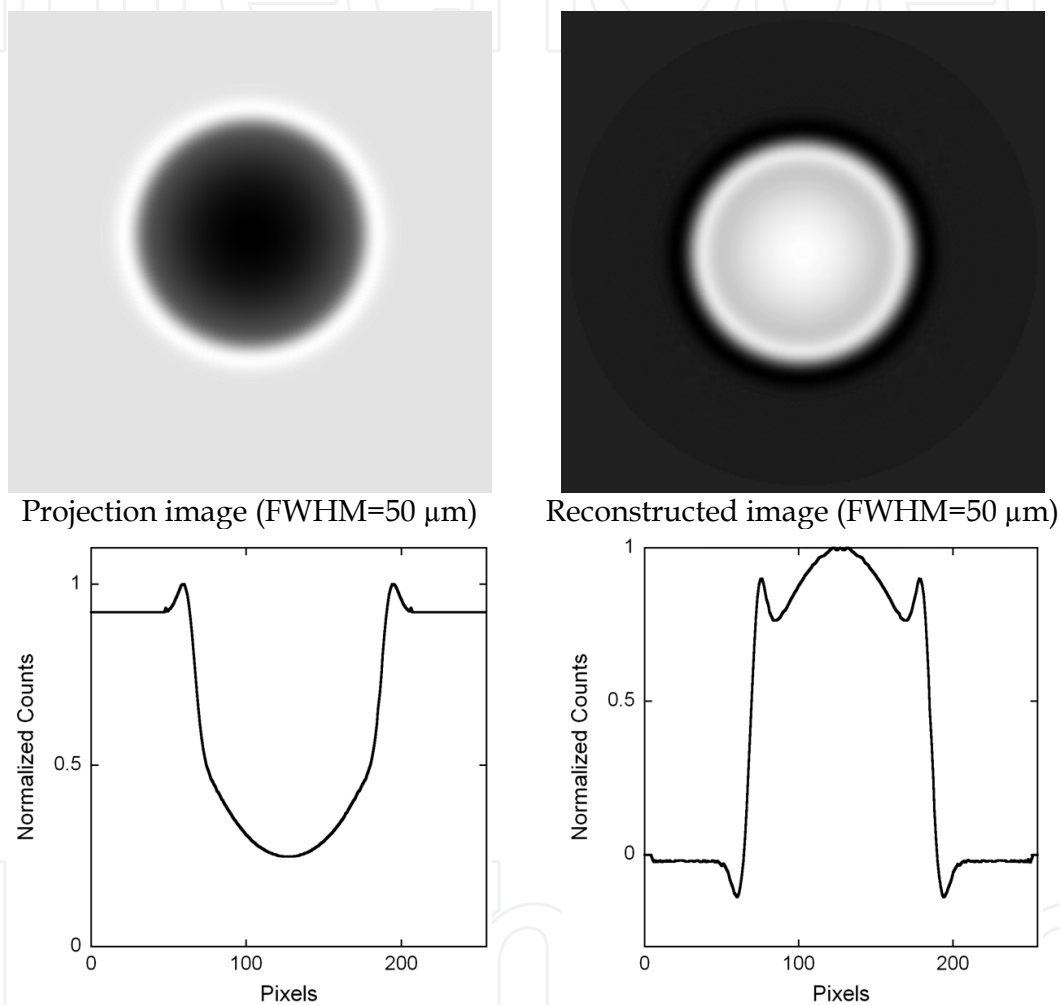

Projection image (FWHM=8 µm)   Reconstructed image (FWHM=8µm)
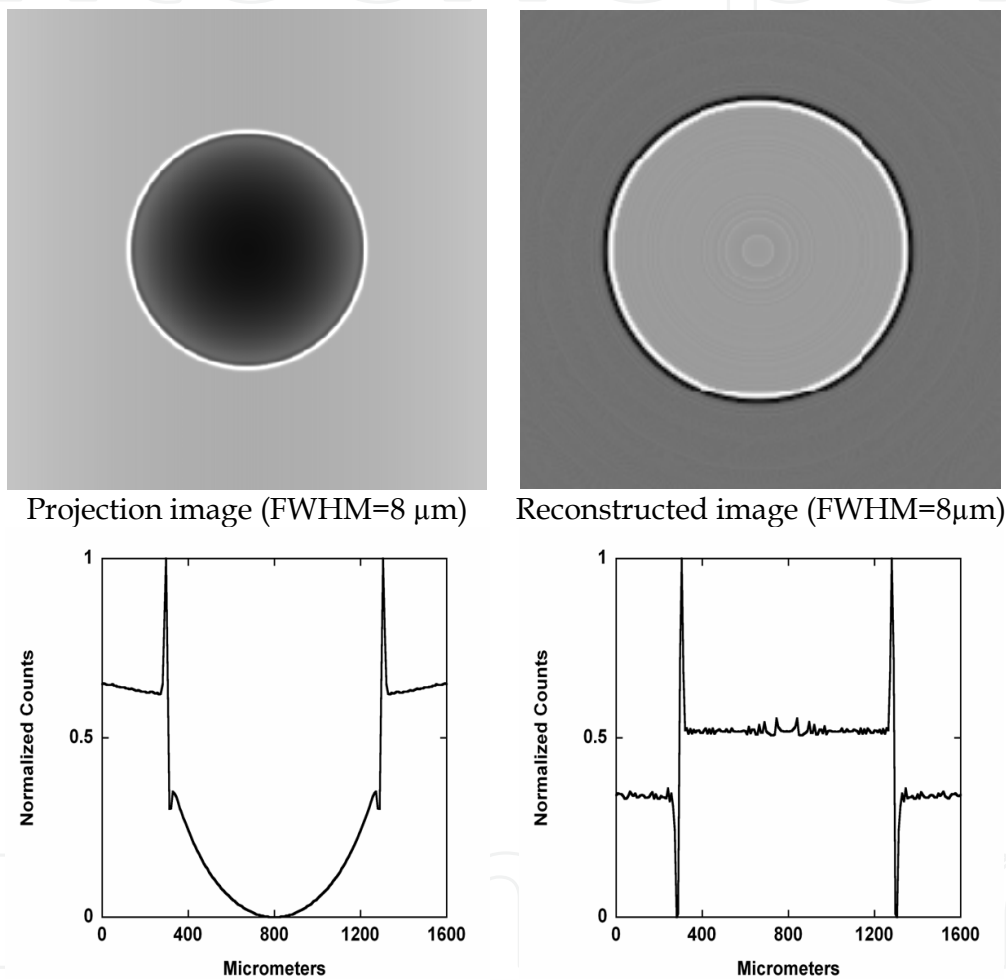
Fig. 7. Simulated projection images (*M*=2) of tumor model using in-line holography geometry. Proliferating cell density distribution FWHM=8µm.

This outer layer was modeled by various degree of Gaussian blurring of density profile across its interface with the surrounding tissue (FWHM in the 8 – 100 µm range). A mouse was approximated by a cylinder 28 mm in diameter and 30 mm in length. The tumor was centrally located and its core had the same radiological properties as the soft tissue and it was embedded in the adipose tissue. The projection approximation was used in simulations i.e. $E_{out}(x,y)$ of the wave transmitted through the object was related to the amplitude $E_{in}(x,y)$ of the wave incident on the object by $E_{out}(x,y) = \exp(i\varphi(x,y) - a(x,y)) E_{in}(x,y)$, where $\varphi(x,y)$ and

$a(x,y)$ are the phase and the attenuation induced by the object, respectively. The free-space propagation from the object plane to the detector was modeled using the rigorous wave-optical formalism (Nesterets et al., 2005). For simplicity, a point source and a perfect detector ($\sigma_S = \sigma_D = 0$) were assumed with $M = 1.1$ and $M = M_{opt} = 2$ (the optimum magnification corresponds to the point source and perfect detector), $R = 2$ m (total source-to-detector distance), and 20 keV x-ray energy. We simulated sets of micro-CT projection images, each consisting of 1440 images and reconstructed them using a modified Feldkamp algorithm (Figs. 7-9).

Fig. 8. Simulated projection images (M=2) of tumor model using in-line holography geometry. Proliferating cell density distribution FWHM=50 μm.

In addition, we estimated absorption and phase-shift image contrast in the projection images of simulated tumor vs. their diameter for different density profiles across its interface with the surrounding tissue (Fig. 10).

We observe phase-shift enhancement of the image contrast at the boundaries of the tumor in the projection images and even stronger enhancement in the reconstructed transaxial images. The enhancement strongly depends on the projected real part of the refractive index gradient at the interface between the tumor and the surrounding tissue. It is very pronounced at FWHM=8 μm, moderate at FWHM=50 μm and difficult to detect at

FWHM=100 µm. At large values of the tumor radii the absorption contrast dominates the phase contrast and the image contrast is therefore independent of the tumor/normal tissue interface blurring. For small tumors (r <1 mm) the phase contrast dominates the absorption contrast but it rapidly decreases with increase of the tumor/normal tissue interface blurring.
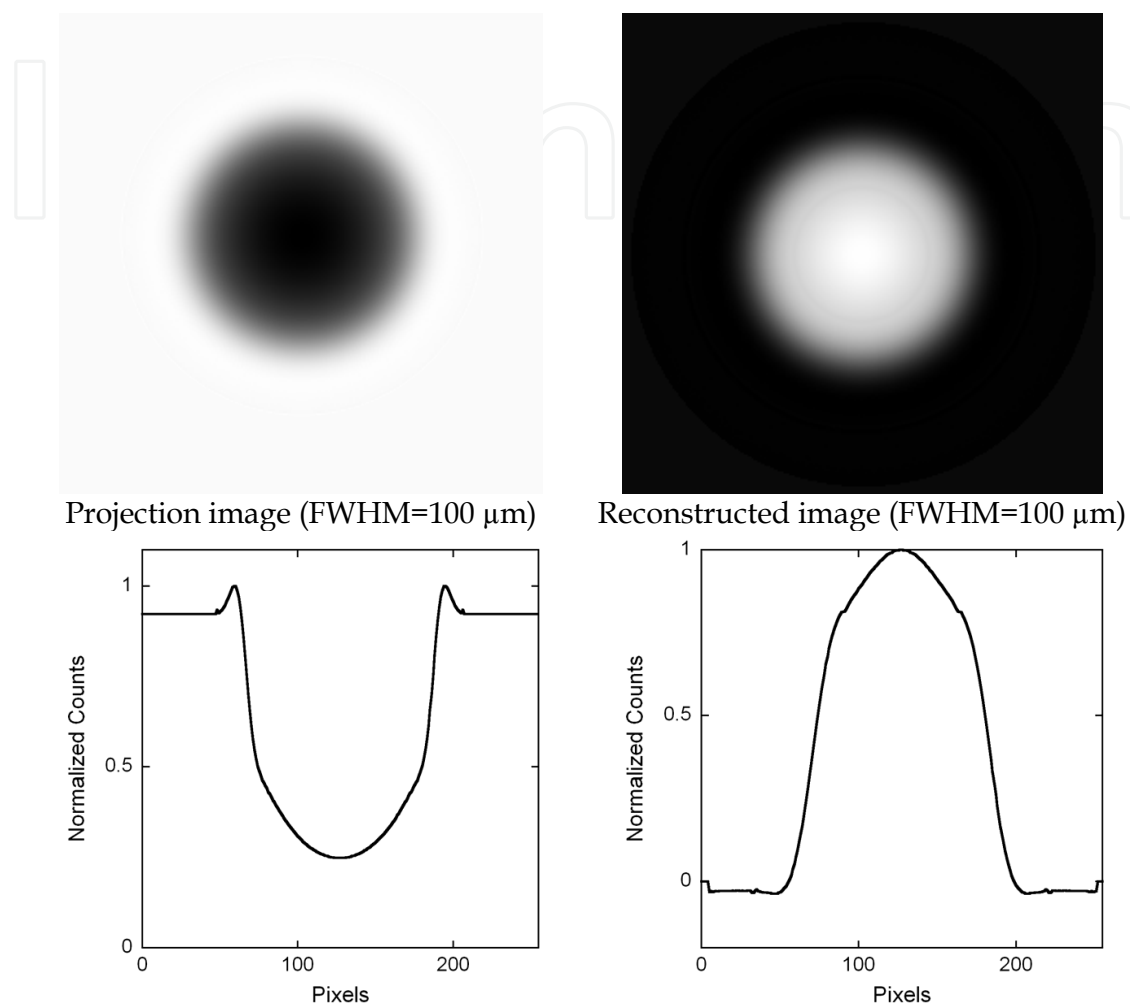

Projection image (FWHM=100 µm)   Reconstructed image (FWHM=100 µm)

Fig. 9. Simulated projection images (M=2) of tumor model using in-line holography geometry. Proliferating cell density distribution FWHM=100 µm.

5. Conclusions

The in-line holography setup for phase-contrast imaging is the simplest and the easiest to implement in the context of biomedical imaging. It does not require high-brilliance x-ray source (e.g. synchrotron) or sophisticated x-ray diffraction crystals or gratings. It does not necessitate narrow x-ray energy band. The field-of-view is limited only by the x-ray detector size but not by the aperture of x-ray optics. The in-line holography is very well suited to detect steep gradients (interfaces) of the real part of the x-ray refraction index inside the object, as well as variation of the imaginary part i.e. x-ray absorption. Consequently, it might allow visualization of internal interfaces, e.g. between normal tissue and tumor (providing that they create sufficient x-ray phase shift) that otherwise do not produce sufficient absorption contrast to be detected in conventional radiological imaging.
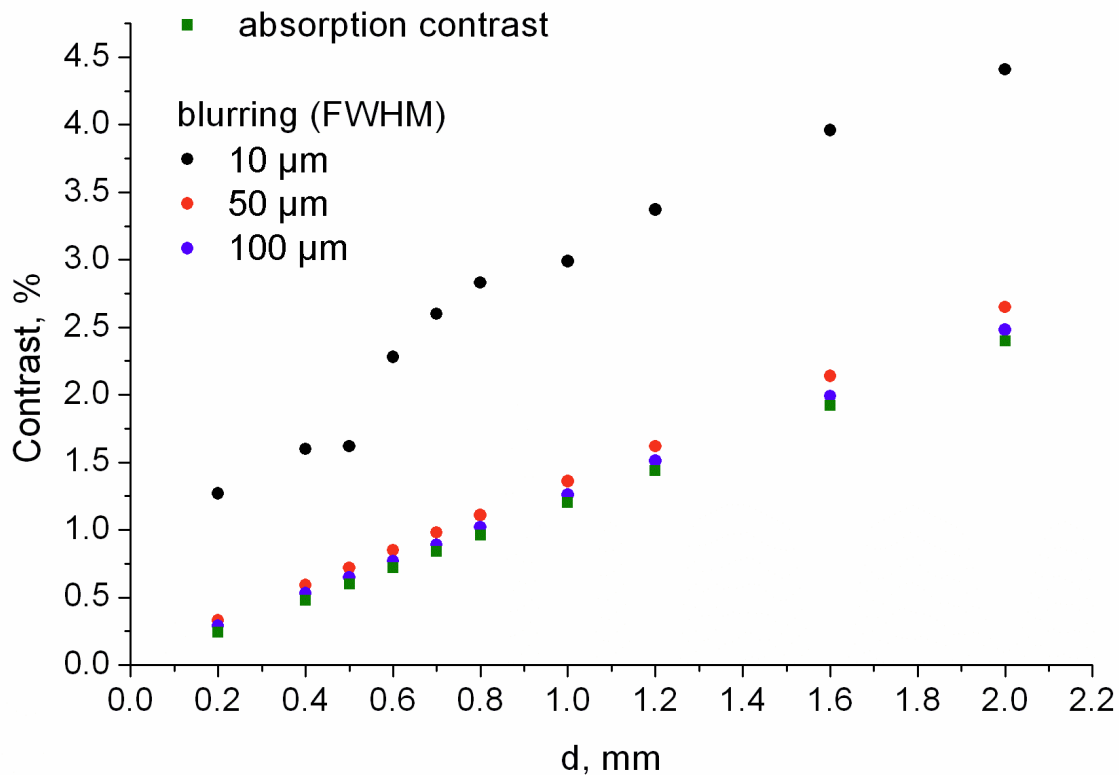
Fig. 10. In-line holography image contrast vs. tumor diameter *d* for proliferating cells for different density profiles across its interface with the surrounding tissue FWHM = 10 μm, 50 μm and 100 μm.

The in-line holography setup requirements include:

i. Sufficiently small x-ray source size to provide required spatial coherence to image the object's component of interest. This condition is met if the shortest spatial wavelength (λ_o) of the feature of interest fulfils the following inequality: $\lambda_o >> s(M-1)/M = s'/M$, where s' is the size of projected source (s) on the detector plane geometrical unsharpness of the system) and M is system magnification.

ii. The x-ray source intensity should match the imaging task, i.e. the x-ray fluence on the sample needs to create minimum acceptable *SNR* and contrast for the imaging task within acceptable exposure time.

iii. The detector sampling (in pixels of the detector) needs to be commensurate with the distance (d_F) between the adjacent minimum and maximum of the intensity due to phase shift in the first Fresnel fringe image of the object. Consequently, one needs at minimum 5 detector pixels to adequately sample the distance d_F.

The above requirements translate into the focal spot size in the 5 –50 μm range depending on the geometrical parameters of the system. The necessary average power of x-ray source depends strongly on the application: 20–100 W for micro-CT, 500–1000 W for breast or chest imaging, and 10–40 kW for whole body CT. Presently, compact x-ray sources that could fulfill some of these conditions include microfocal x-ray tube and ultrafast laser-based x-ray source. However, micro-focal x-ray tube suffers from maximum power limit imposed by the required small focal spot size and could be used for micro imaging only. It also produces rather broad x-ray spectra that are difficult to tune. Ultrafast lasers on the other hand, are

fast evolving technology and it is expected that they will reach kilowatt average power level within the next ten years. Presently, they could be used for micro (preclinical) imaging. The x-ray spectra produced by ultrafast laser-based x-ray source can be easily tuned by change of the target elemental composition and could be optimized for the specific imaging task. The required pixel size of the detector is in the 5 – 30 μm range, depending on the system parameters. The ongoing progress in the field of radiological x-ray detectors will lead to creation of large-area high-resolution, low-noise, photon-counting detectors that would match requirements of clinical in-line holography x-ray imaging systems.

6. References

Als-Nielsen, J. and McMorrow, D. (2001). *Elements of Modern X-Ray Physics*, Chichester: Wiley.

Bilderback, D.H,; Elleaume, P.; Weckert E. (2005). Review of third and next generation synchrotron light sources. *J Phys B At Mol Opt Phys*, 38, pp S773-97.

Chapman, D.; Thomlinson, W.; Johnston, R. E., Washburn, D.; Pisano, E.; Gmur, N.; Zhong, Z.; Menk, R.; Arfelli, F.; Sayers, D. (1997). *Phys. Med. Biol.,* 42, pp 2015–25.

Grubel, G.; Stephenson, G.B.; Gutt, C.; Sinn, H.; Tschentscher, T. (2007). XPCS at the European X-ray free electron laser facility, *Nucl Instrum Methods Phys Res,* B262, pp. 357-67.

Gureyev, T.E. & Wilkins, S.W. (1998). On X-ray phase retrieval from polychromatic images, *Optics Communications*, 147, pp. 229-232.

Kieffer, J.C.; Krol, A.; Jiang, Z.; Chamberlain, C.C.; Scalzetti, E.; Ichalalene, Z. (2002). Future of Laser-Based X-Ray Sources for Medical Imaging", *J. Appl. Phys. B*, 74, pp. S75-S81.

Jiang, Y.; Pjesivac-Grbovic, J.; Cantrell, C.; Freyer, J.P. (2005). A Multiscale Model for Avascular Tumor Growth, *Biophysical Journal*, 89, pp. 3884–3894.

Krol, A.; Kincaid, R.; Servol, M.; Kieffer, J.C.; Nesterets, Y.; Gureyev, T.; Stevenson, A.; Wilkins, S.; Ye, H.; Lipson, E.; Toth, R.; Pogany, A.; Coman, I. (2007). Initial experimentation with in-line holography x-ray phase-contrast imaging with an ultrafast laser-based x-ray source, *Proc SPIE,* 6510, pp. 65100L.

Lewis, R.A. (2004). Medical phase contrast X-ray imaging: current status and future prospects. *Phys Med Biol,* 49, pp. 3573-83.

Lohmann, A. W; & Silva, D. E. (1971). Opt. Commun. 2, pp. 413.

Momose, A. (1995). Demonstration of phase-contrast computed tomography using an X-ray interferometer, *Nucl Instrum Methods* A352:622-8.

Momose, A.; Takeda, T.; Itai, Y.; Hirano, K. (1996). Phase-contrast x-ray computed tomography for observing biological soft tissues, *Nat. Med.*, 2, pp. 473–5.

Momose, A. & Fukuda, J. (1995). *Med. Phys.*, 22, pp. 375.

Momose, A.; Takeda, T,; Itai, Y. et al. (1998). *J. Synchrotron Radiat.,* 5, pp. 309–14.

Momose, A. (2002). Phase-contrast X-ray imaging based on interferometry, *J Synchrotron Rad* 9, pp. 136-42.

Momose, A. (2003). Phase-sensitive imaging and phase tomography using X-ray interferometers, *Opt Expr*, 11(19) pp. 2303-14.

Momose, A.; Yashiro, W.; Takeda, Y.; Suzuki, Y.; Hattori, T. (2006). Phase tomography by x-ray Talbot interferometry for biological Imaging, *Japan. J. Appl. Phys.*, 45, pp. 5254–62.

Nesterets, Y.I.; Gureyev, T.E.; Paganin, D.; Pavlov, K.M.; Wilkins, S.W. (2004). Quantitative diffraction-enhanced X-ray imaging of weak objects, *J Phys D Appl Phys*, 37, pp. 1262-74.

Nesterets, Y.I.; Wilkins, S.W.; Gureyev, T.E.; Pogany, A.; Stevenson, A.W. (2005). On the optimization of experimental parameters for x-ray in- phase-contrast imaging, *Rev. Sci. Instr.*, 76, 093706.

Nesterets,Y.; Gureyev, T.; Stevenson, A.; Pogany,A.; Wilkins, S.; Kincaid, R.; Ye, H.; Vogelsang, L.; Lipson, E.; Coman, I.; Fourmaux, S.; Kieffer, J.C.; Krol, A. (2008). Soft tissue small avascular tumor imaging with x-ray phase-contrast micro-CT in in-line holography setup, *Proceedings of SPIE*, 6913.

Nugent, K.A.; Paganin, D.; Gureyev, T. E. (2001). The phase odysse, *Physics Today*, pp. 27-32.

Olivo, A. & Speller, R. (2007). A coded-aperture technique allowing X-ray phase contrast imaging with conventional sources, *Appl Phys Lett*, 91, pp. 074106

Pfeiffer, F.; Weitkamp, T.; Bunk, O.; David, C. (2006). Phase retrieval and differential phase-contrast imaging with low-brilliance x-ray sources, *Nat. Phys.*, 2, 258–61.

Stein, M.A.; Demuth, T.; Mobley, D. et al.(2007). A Mathematical Model of Glioblastoma Tumor Spheroid Invasion in a Three-Dimensional In Vitro Experiment, *Biophysical Journal*, 92, pp. 356–365.

Pogany, A.; Gao, D.; Wilkins, S.W. (1997). Contrast and resolution in imaging with a microfocus x-ray source, *Rev. Sci. Inst.* 68, pp. 2774-2782.

Rigon, L.; Arfelli, F.; Menk, R.H. (2007). Three-image diffraction enhanced imaging algorithm to extract absorption, refraction, and ultrasmall-angle scattering. *Appl Phys Lett*, 90, pp. 114102.

Snigirev A, Snigireva I, Kohn V, Kuznetsov S, Schelokov I. On the possibilities of X-ray phase contrast microimaging by coherent high-energy synchrotron radiation. Rev Sci Instrum 1995;66:5486-92.

Takeda, T.; Wu, J.; Lwin, T. T.; et al. (2007). Interferometer-based phase-contrast X-ray computed of colon cancer specimens: comparative study with 4.74-T magnetic resonance imaging and optical microscopy, *J Comput Assist Tomogr*, 31, pp. 214-7.

Weitkamp, T.; Diaz, A.; David, C.; et al. (2005). X-ray phase imaging with a grating interferometer, *Opt. Exp.*, 13, pp. 6296–304.

Weitkamp, T; David, C.; Kottlerb, C.; Bunkc, O.; Pfeiffer, F. (2006). Tomography with grating interferometers at low-brilliance sources, *Proc. SPIE*, 6318.

Wernick, M.N.; Wirjadi, O., Chapman D, et al.(2003). Multiple-image radiography. *Phys Med Biol*, 48, pp. 3875-95.

Wilkins, S.W.; Gureyev, T.E.; Gao, D.; Pogany, A.; Stevenson, A.W. (1996). Phase-contrast imaging using polychromatic hard X-rays. *Nature*, 384, pp. 335-8.

Yokozeki, S. & Suzuki, T. (1971). *Appl. Opt.*, 10, pp. 1575.

Wu, X.; & Liu, H. (2007). Clarification of aspects in in-line phase-sensitive, X-ray imaging., *Med Phys*, 34(2), pp. 737-43.

Zhang, X.; Liu, X.S.; Yang, X.R. et al. (2008). *Phys. Med. Biol.*, 53, pp. 5735–5743

Zhou, S.; & Brahme, A., (2008). Development of phase-contrast X-ray imaging techniques and potential medical applications, *Physica Medica,* 24, pp. 129-148.

Holography, Research and Technologies

Edited by Prof. Joseph Rosen

ISBN 978-953-307-227-2

Hard cover, 454 pages

Publisher InTech

Published online 28, February, 2011

Published in print edition February, 2011

Holography has recently become a field of much interest because of the many new applications implemented by various holographic techniques. This book is a collection of 22 excellent chapters written by various experts, and it covers various aspects of holography. The chapters of the book are organized in six sections, starting with theory, continuing with materials, techniques, applications as well as digital algorithms, and finally ending with non-optical holograms. The book contains recent outputs from researches belonging to different research groups worldwide, providing a rich diversity of approaches to the topic of holography.

INTECH
open science | open minds